Nuclear Instruments and Methods in Physics Research A 788 (2015) 86–94

Contents lists available at ScienceDirect

Nuclear Instruments and Methods in Physics Research A

journal homepage: www.elsevier.com/locate/nima

Evaluation of a high resolution silicon PET insert module

Milan Grkovski [a,b,*], Karol Brzezinski [c], Vladimir Cindro [a], Neal H. Clinthorne [d], Harris Kagan [e], Carlos Lacasta [c], Marko Mikuž [a], Carles Solaz [c], Andrej Studen [a], Peter Weilhammer [e], Dejan Žontar [a]

[a] *Jožef Stefan Institute, Ljubljana, Slovenia*
[b] *Memorial Sloan Kettering Cancer Center, New York, NY, USA*
[c] *IFIC/CSIC, Valencia, Spain*
[d] *University of Michigan, Ann Arbor, MI, USA*
[e] *Ohio State University, Columbus, OH, USA*

ARTICLE INFO

Article history:
Received 29 October 2014
Received in revised form
26 March 2015
Accepted 29 March 2015
Available online 8 April 2015

Keywords:
Positron emission tomography
Silicon detectors
PET insert
Image reconstruction

ABSTRACT

Conventional PET systems can be augmented with additional detectors placed in close proximity of the region of interest. We developed a high resolution PET insert module to evaluate the added benefit of such a combination. The insert module consists of two back-to-back 1 mm thick silicon sensors, each segmented into 1040 1 mm^2 pads arranged in a 40 by 26 array. A set of 16 VATAGP7.1 ASICs and a custom assembled data acquisition board were used to read out the signal from the insert module.

Data were acquired in slice (2D) geometry with a Jaszczak phantom (rod diameters of 1.2–4.8 mm) filled with ^{18}F-FDG and the images were reconstructed with ML-EM method. Both data with full and limited angular coverage from the insert module were considered and three types of coincidence events were combined.

The ratio of high-resolution data that substantially improves quality of the reconstructed image for the region near the surface of the insert module was estimated to be about 4%. Results from our previous studies suggest that such ratio could be achieved at a moderate technological expense by using an equivalent of two insert modules (an effective sensor thickness of 4 mm).

1. Introduction

Whole-body PET scanners have evolved considerably in the recent decade, but still offer relatively poor volumetric resolution, compromising their ability of quantifying radiotracer uptake [1,2]. Improvements in spatial resolution of PET detectors can be attained through finer segmentation of detector elements [3]. However, the achievable spatial resolution will be limited by positron range and acollinearity of annihilation photons, the latter being dependent on the distance between the annihilation point and detector elements [3].

The performance of a whole-body PET scanner may be augmented by using an additional high resolution insert. Such configuration would enhance photon sensitivity by increasing the system's geometric detection efficiency [4], and improve its spatial resolution. A number of multi-resolution PET concepts have been investigated by several groups, utilizing either semiconductor materials such as silicon [5–9] and cadmium zinc telluride (CdZnTe) [10,11] or scintillators such as cerium-doped lutetium (-yttrium) oxyorthosilicate (L(Y)SO) [12–16], usually read out by silicon photomultipliers (SiPMs).

The proposed approach implies placement of additional detectors (*inserts*) within the existing scanner ring. As a result, a mixture of events of different modes is collected simultaneously: standard ring–ring interactions, events where one of the annihilation photons interacts in the insert and the remaining one in the ring (insert–ring) and possibly, should the geometry of the insert allow, insert–insert interactions. Such strategy is feasible only if spatial resolution of the insert sufficiently surpasses the resolution of the baseline scanner.

In the approach investigated by our group [17–19], high resistivity silicon sensors segmented to individual pads were chosen as the detector material for the insert, offering excellent spatial [20] and energy resolution [21]. Silicon-based detectors should be insensitive to operation in a magnetic field [22], enabling the employment of PET inserts for MRI [23] and, due to their segmentation, are not expected to be susceptible to mis-localization of annihilation photons (depth-of-interaction (DOI) effect).

---

[*] Corresponding author at: Memorial Sloan Kettering Cancer Center, New York, NY, USA.
E-mail address: milan.grkovski@ijs.si (M. Grkovski).

http://dx.doi.org/10.1016/j.nima.2015.03.078
0168-9002/

We developed a high resolution silicon PET insert module, building block for the insert concept. The aim of the present study was to characterize image quality of each coincidence type and determine portions of additional events (insert–ring, insert–insert) required for improved image quality. As PET inserts can cover only a portion of the object, geometries where image quality is maintained despite limited angular coverage was investigated. While silicon might not be the definitive material for PET insert application, it satisfies the crucial requirement for the insert, the high spatial resolution. In that sense the results are indicative for other semiconductor materials or scintillator-SiPM assemblies able to achieve such spatial resolution. We were also guided by availability, robustness and knowledge of operation. Some drawbacks, including limited efficiency, timing and event classification difficulties, are addressed in the discussion.

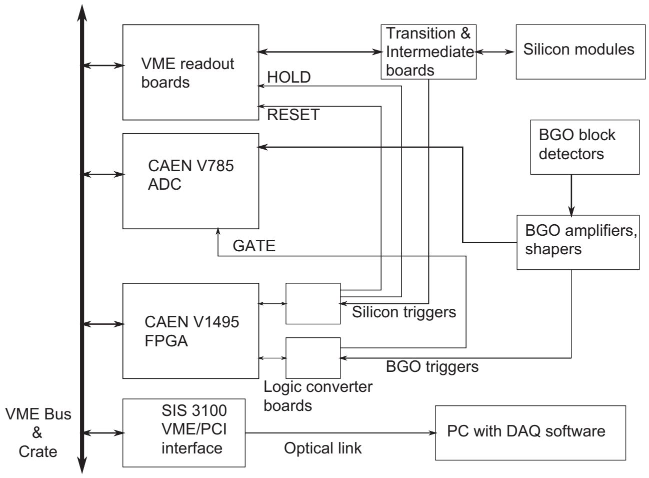

Fig. 2. Schematic drawing of the data acquisition system for the evaluation setup. During the measurements, insert modules were used in parallel with the outer ring.

2. Materials and methods

2.1. PET insert module

The PET insert module (or 'module', shown in Fig. 1) consists of a single pair of 1 mm thick silicon sensors manufactured by SINTEF (SINTEF Group, Norway), each segmented into 1040 1 mm^2 pads. Each pad is a diode with a p^+nn^+ doping profile, and the pads are arranged in a two-dimensional mesh (40 by 26). The two sensors are placed 0.8 mm apart in a back-to-back configuration and are glued to two double-sided hybrids. Silicon sensors were operated at 136 V bias (full depletion occurs at ~100 V). The insert can be composed of several modules.

The VATAGP7.1, 128 readout channel low noise application-specific integrated circuit (ASIC), designed and fabricated by IDEAS (Integrated Detector and Electronics (IDE) AS, Norway), was employed as the front-end electronics for the module. Individual readout channels consist of a common charge sensitive preamplifier with its output split to an analog (VA) and a digital (TA) branch. The VA branch consists of a noise filtering slow semi-Gaussian CR-RC shaper with adjustable a shaping time of 500 ns. The shaper is followed by a Sample & Hold circuit, triggered by external electronics. The ASIC provides a sparse-adjacent readout mode where only the hit channel along with a number of adjacent channels is read out. In our case, 15 adjacent channels were used to estimate common mode noise of the ASIC. The TA branch consists of a fast CR-RC shaper (150 ns shaping time) followed by leading edge discriminator and a monostable that produces a trigger if the signal exceeds the externally set threshold voltage. A single module is read out by 16 chips embedded on two double-sided hybrids also providing mechanical support for the sensors.

From hybrid, the signals are relayed through transition board to the intermediate board (IB) which serves as an additional amplification and analog control unit for every hybrid. The final unit of the silicon readout is a VME (Versa Module Eurocard)-compatible board providing analog to digital conversion and digital processing of the event. The packaged events are then sent through VME back-end and VME-PC optical link to the personal computer serving as slow control, storage and processing unit (Fig. 2).

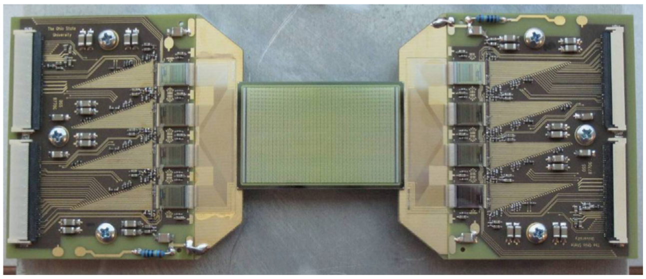

Fig. 1. Silicon insert module. Two sensors are placed in a back-to-back configuration (second sensor not visible) and glued to two double-sided hybrids, where ASICs are hosted.

By default, readout chain is started by trigger from the ASIC. For coincidence operation this chain is broken via on-board switch, and the IB provides buffered trigger signal available for coincidence logic, which should either provide a confirmation through a readout trigger or a reset indicator otherwise. The IB serves as the reception port for both signals and relays the reset to the hybrid and ASICs.

The modules were characterized prior to tests in PET geometry [24]. In terms of timing, time-walk similar to TA branch shaping time of ~150 ns was found to be the dominant contribution. Additional contribution comes from variation in pulse shape with interaction location, adding up to ~50 ns timing uncertainty at moderate biases used in the setup.

The measured energy resolution was 2.5 keV full width at half maximum (FWHM) at 60 keV ^{241}Am photo-peak [25]. Nevertheless, sensors are normally operated in open mode for 511 keV photons, that is accepting any interaction type, because of the low probability of the photo-electric absorption. Stable operation was achieved for thresholds above ~20 keV. Both timing and energy spectra of silicon detectors measured in the coincidence setup are shown in Fig. 3.

Either a partial or a full ring can be constructed using multiple modules. A full inner ring can be assembled by combining several modules in a circular arrangement, providing near-complete angular coverage. Both concepts are illustrated in Fig. 4. The naming convention of the interaction types refers to the detectors used in our evaluation setup (i.e., 'Si' for silicon and 'BGO' for bismuth germanate scintillator detectors used in outer ring). Two additional types of coincidence events are available when using a full inner ring: high resolution Si–BGO events (where one of the annihilation photons interacts in the module and the other is detected in the outer scintillator ring) and very high resolution Si–Si events (where both annihilation photons interact in modules).

2.2. Evaluation setup

Schematic drawing of the evaluation setup used to acquire the data is shown in Fig. 5. The setup consists of a partial BGO ring mimicking standard PET detectors, rotating table for imaging

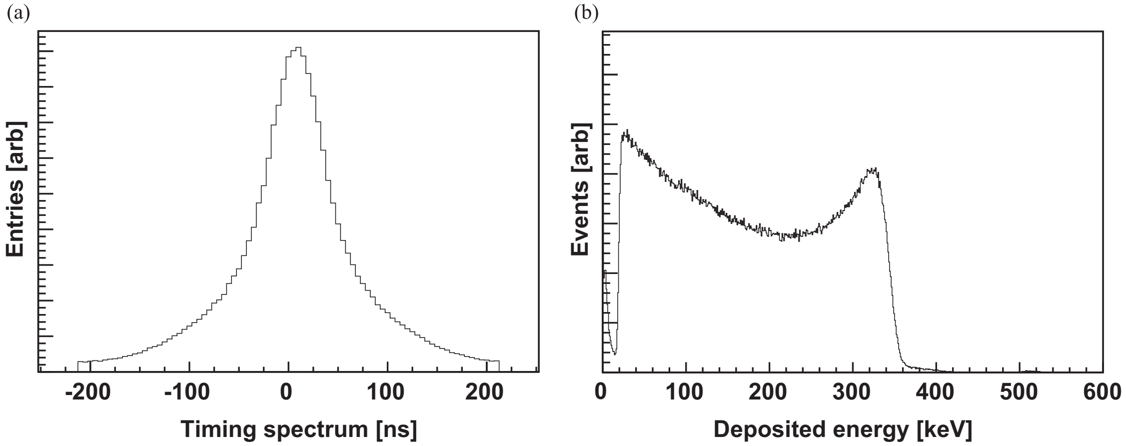

Fig. 3. Timing (a) and energy (b) spectra of silicon detectors.

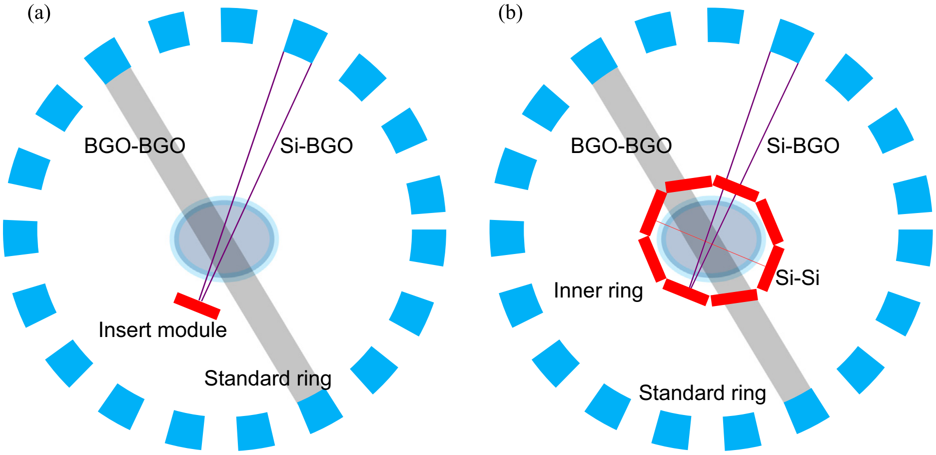

Fig. 4. Illustration of the two applications of silicon detectors under investigation by our group. Insert concept (a) and full inner ring assembled with multiple modules (b). Two or three types of coincidences are available, depending on the concept: standard moderate resolution BGO–BGO (ring–ring) events, high resolution Si–BGO (insert–ring or, alternatively, inner ring–outer ring) events and very high resolution Si–Si (inner ring–inner ring) events.

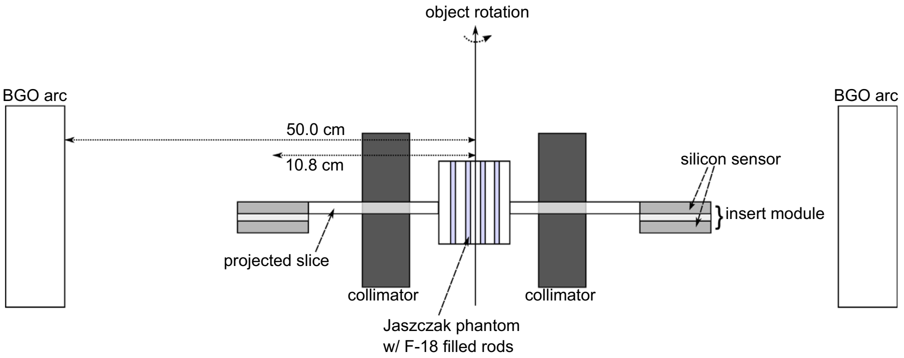

Fig. 5. Schematic drawing of the single slice geometry for the evaluation setup. Dimensions are not drawn to scale. Only one of the two silicon sensors was used to detect coincidence events. The silicon sensor is in edge-on geometry to increase the effective thickness and thus the detection efficiency, whereas in a clinical application it would remain in face-on geometry (as shown in Fig. 4).

objects, collimators and mechanical gantry for inserts where silicon modules were placed.

2.2.1. Partial BGO ring

A total of 24 BGO block detectors (scavenged from a CTI 931 PET scanner) were arranged in 2 arcs, with each arc covering 67.5° relative to the rotary table located at the arc center. The inner radius of the arc was 50 cm. Each BGO block is a segmented 4×8 array of 5.25 mm × 12.5 mm, 30 mm thick BGO crystals enveloped in a protective gantry and read out by a 2×2 array of Hamamatsu R2497 photomultipliers (PMTs). Spatial resolution of the BGO detectors is around 6.5 mm FWHM circumferentially and 13 mm FWHM axially.

Output of block detectors was routed to a custom built amplifier board that was used to generate triggers via leading

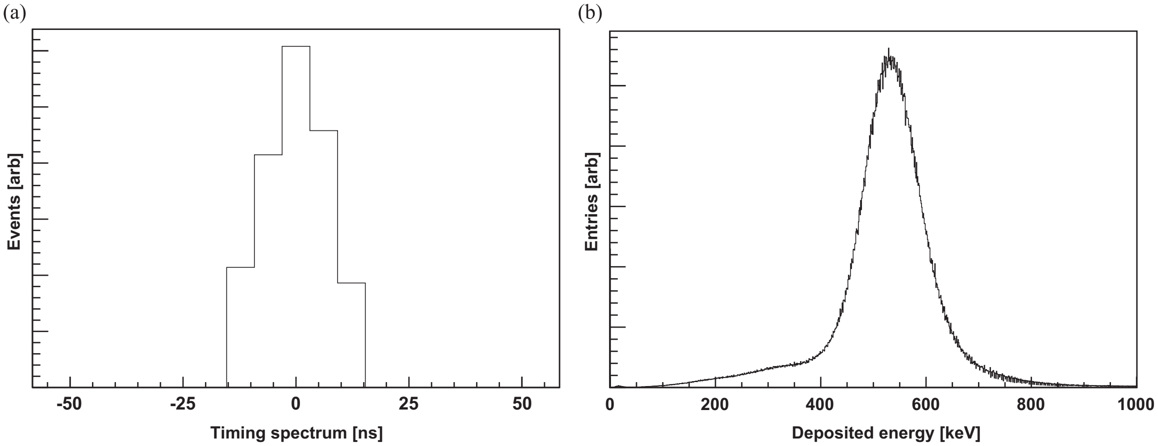

Fig. 6. Timing (a) and energy (b) spectra of BGO detectors.

edge discriminator using sum of the signal from all four PMTs as an input for coincidence processing and buffer signals for VME-based CAEN V785 peak sensing analog-to-digital converter (ADC). A gate was sent to the V785 to detect and convert the signal peak values coming from the PMTs (Fig. 2). The timing and energy spectra of BGO detectors are shown in Fig. 6. Timestamps were applied by the 5 ns granulated time-to-digital converter, and the timing resolution of 5 ns FWHM was estimated. The energy threshold was set to ~300 keV, with small variations between individual crystals.

2.2.2. *Imaging geometry*

Rotary table was set at the center of the partial BGO ring (Fig. 5). Lead blocks and tungsten leafs surrounded the table, collimating the field of view (FOV) to a ~1.5 mm thick horizontal slice through the object. The silicon modules were oriented edge-on and shifted vertically so that only one of the two back-to-back sensors was aligned with the collimated slice. This geometry simulates a thicker silicon sensor, thus compensating for silicon's low stopping power, and reduces the contribution of single or scattered photons originating from outside of the imaged slice. The distance between the center of the silicon sensors and the center of rotation was 10.8 cm.

A Micro Hot Spot Insert Jaszczak phantom with rod diameters of 1.2, 1.6, 2.4, 3.2, 4.0 and 4.8 mm was fixed to the rotary table, with rods oriented vertically. For each run, the phantom was filled with a solution of ^{18}F-FDG with specific activity of 40 MBq/ml (~18 MBq within collimated slice). To approximate a uniform angular distribution of collected data, phantom was rotated through 20 full rotations in 6° steps with a dwell time of 15 s per step. Typically, 14 M BGO–BGO, 3 M Si–BGO and 700k Si–Si events were collected per dedicated run. For larger statistics, runs were coherently combined yielding a total of 9.1 M and 8.4 M collected Si–BGO and Si–Si events, respectively. All measurements were performed in an air conditioned environment at the room temperature of 21° C.

2.3. *Coincidence logic*

A field programmable gate array (FPGA) circuit on the CAEN V1495 VME modules was used to combine trigger signals from individual silicon modules and BGO detectors (Fig. 2). The module also emitted readout triggers and reset signals for silicon and BGO subsystems. Using internal 5 ns global clock, the FPGA also served as a timing device.

For a valid coincidence, a Si interaction opened a 250 ns long coincidence window and BGO interaction a 5 ns window. Effective window durations were hence 500 ns for Si–Si, 255 ns for Si–BGO and 10 ns for a BGO–BGO events.

For valid events, a readout trigger was sent to the respective IB, and gate for V785 VME module was generated. Otherwise, all silicon modules were reset and new interaction was awaited.

The timing information recorded by the coincidence module consisted of relative delay of received triggers and global time stamp. For a valid event, data from all VME modules (V785, V1495 and silicon VME board) were sent sequentially to the receiving PC. After the data has been read from all VME modules, a reset signal was sent to the FPGA to prepare the system for a new event. With this strategy, event rate was limited to ~300 Hz. Although simultaneous collection of all event types was possible, limited event rate forced us to dedicated runs to improve statistics of Si–Si and Si–BGO events.

2.4. *Multi-resolution image reconstruction*

Point spread function (PSF) in direction transverse to the line of response was modeled by convolving the contributions of [26]

- Detector spatial resolution, a convolution of uniform distributions of each pad/crystal [12], calculated at the center of the rotary table as an approximation of the annihilation location.
- Positron range, modeled as a bi-exponential curve, with coefficients taken from [27].
- Annihilation photon acollinearity, having a Gaussian distribution with zero mean and a FWHM of $R_{acol} = ((x \cdot (D-x))/D) \cdot 0.0088$, where D is the separation between detector elements and x is the distance between the detector element and the point of annihilation, approximated by the center of the rotary table. The unknown annihilation position also prompted approximation of detector element location with the centers of respective detector systems, that is modules and arcs.

The PSFs were verified through images of ^{22}Na point sources reconstructed with filtered backprojection, and excellent match was found [26]. PSFs were included in the system model through radial convolution of the measured sinograms, while angular spread was assumed smaller than the sinogram angle bin.

Maximum likelihood expectation maximization (ML-EM) method [28] was used for multi-resolution image reconstruction. The likelihood function was written as the sum of the contributions of the individual types of coincidence events. For every coincidence type, the PSF outline above and sensitivity scaled to the count of a particular event type were used. The iterative process is given by

$$\hat{f}_j^{n+1} = \hat{f}_j^{n} \frac{\left(\sum_i H_{ij}^{s} \frac{p_i^{s}}{\sum_k H_{ik}^{s} \hat{f}_k^{n}} + \sum_i H_{ij}^{sb} \frac{p_i^{sb}}{\sum_k H_{ik}^{sb} \hat{f}_k^{n}} + \sum_i H_{ij}^{b} \frac{p_i^{b}}{\sum_k H_{ik}^{b} \hat{f}_k^{n}} \right)}{\left(\sum_{i'} H_{i'j}^{s} + \sum_{i'} H_{i'j}^{sb} + \sum_{i'} H_{i'j}^{b} \right)} \qquad (1)$$

where p_i are the measurements, $H=(H_{ij})$ is the system matrix, $\hat{f}_j^{n+1}$ ($\hat{f}_j^{n}$) is the new (current) image estimate and $\sum_{i'} H_{i'j}$ is the scanner sensitivity in voxel j. Superscripts s, sb and b designate Si–Si, Si–BGO and BGO–BGO coincidences, respectively. Due to their relative low frequency in the acquired dataset, random and scattered coincidences were omitted from the above equation.

Sinograms (bin sizes of 200 μm and 0.9°) were reconstructed using ML-EM with the system model as described. A 1000 iterations were performed for each reconstruction to allow for the convergence of the solution, thus limiting the impact of reconstruction process on the reconstructed image. Smoothing with a Gaussian kernel ($\sigma = 0.4$ mm) was applied at the end of the iteration procedure, partially compensating for a spatially variant PSF of ML-EM.

Mean squared error (MSE) was used to estimate reconstructed image quality [26], and was defined as

$$MSE = \sum_i \left(\frac{1}{q} \varrho_i - f_i \right)^2 \qquad (2)$$

where ϱ_i is the reconstructed activity in pixel i, f_i is the true activity of a Jaszczak phantom used in the measurements, assuming a source density of 1 within the rods and 0 elsewhere, and q is a scaling factor, defined as

$$q = \frac{\sum_i \varrho_i}{\sum_i f_i}. \qquad (3)$$

Summation was performed over all pixels within the field of view, chosen as 40 mm diameter circle matching the size of the silicon sensor. By using the same phantom, image reconstruction method, convergence criteria and smoothing, the impact of reconstruction method was minimized, such that the reconstructed images mostly reflect the different spatial resolution of the included coincidences.

3. Results

3.1. Single event type reconstruction

ML-EM was used to reconstruct the images from single event type data a, with Eq. (1) rewritten as

$$\hat{f}_j^{n+1} = \hat{f}_j^{n} \frac{\left(\sum_i H_{ij}^{a} \frac{p_i}{\sum_k H_{ik}^{a} \hat{f}_k^{n}} \right)}{\left(\sum_{i'} H_{i'j}^{a} \right)}. \qquad (4)$$

An improvement in image quality is demonstrated in Fig. 7, where reconstructions from all three types of events are shown, using approximately the same number of events in each case. In the image reconstructed from BGO–BGO coincidences only, 4.8 mm, 4.0 mm and 3.2 mm rods can be resolved and the calculated MSE value was 6.0. Image quality as obtained from Si–BGO coincidences only is visibly better as both 2.4 mm and 1.6 mm rods can be resolved (MSE = 4.1). Further improvement can be appreciated in the image reconstructed from Si–Si coincidences only, where also the 1.2 mm rods can be clearly resolved (MSE = 3.3). For each reconstructed image, only one type of coincidence events was considered to demonstrate the differences in obtainable spatial resolution. In a clinical situation, acquired dataset would be comprised predominantly of ring–ring (BGO–BGO) coincidences, as detectors in the outer ring outperform smaller high-resolution detector both in terms of angular coverage and in detection efficiency.

3.2. Effect of adding higher resolution data

The effect of adding different amounts of Si–BGO and Si–Si events (with full angular coverage) to standard BGO–BGO events is illustrated in Fig. 8. 2.4 mm rods on the images reconstructed with the addition of Si–BGO events can be resolved when including ~3% of such events. The improvement in image quality is pronounced further when augmenting BGO–BGO data with Si–Si events, as by including ~3% of those events, even the smallest 1.2 mm rods are resolvable.

MSE values, calculated for various combinations of the percentage of high-resolution information added to lower resolution data, are shown in Fig. 9. Improvement in reconstructed image quality is already appreciable by using only a few % of higher resolution events, with Si–Si data (black curve) showing more impact when compared to using the same amount of Si–BGO data (blue curve). The added benefit abates once the ratio of higher resolution events reaches about 10%. When augmenting Si–BGO data (red curve), the beneficial effect only becomes pronounced after including more than 5% of Si–Si information, as the difference between the inherent spatial resolution of the two coincidence types is smaller. The unexpected advantage of Si–Si augmented BGO–BGO data over Si–Si augmented Si–BGO data indicates limitations of the evaluation algorithm stemming from limited accuracy of PSF modeling, different solid angles of silicon and BGO detectors, effects of digitization and other minor factors.

3.3. Effect of a limited angular coverage

The results from the previous section show that a significant improvement in the combined PET system performance can be expected for relatively low fractions of higher resolution information. However, full angular coverage of modules was assumed, a prerequisite that cannot be readily realized in clinical imaging.

If a single module is used that remains stationary during data acquisition, improvement in resolution can only be observed in the direction parallel to the sensor surface [29]. Rather than rotating a single module around the region of interest, a more convenient solution may be to use multiple modules placed at variable angles with respect to each other, depending on the clinical application. Artifacts related to limited angular coverage can be reduced by using two modules at different angular locations. Perpendicular setting was used for illustration. In principle, the angle between the two modules can be adjusted closely to envelop the surface of the patient.

Reconstructions obtained from such layout are shown in Fig. 10a–c. Location of modules is indicated with green rectangles in Fig. 10(b) and (c) while Fig. 10d shows an arrangement in a possible application for elongated objects. Events were retrospectively extracted from full-angle dataset by including only information from seven angular positions (0° ± 18° in 6° steps) and the perpendicular placement of the two modules was simulated by combining information from two initial positions of the module (i.e. 0° and 90°). The same number of higher resolution events is used for both reconstructions. Positions of the two modules are for illustrative purposes highlighted in green. The image in Fig. 10b (MSE = 4.9) is comparable to that in Fig. 8a (MSE = 4.9), which was achieved by using same amount of higher resolution information, but with full angular coverage.

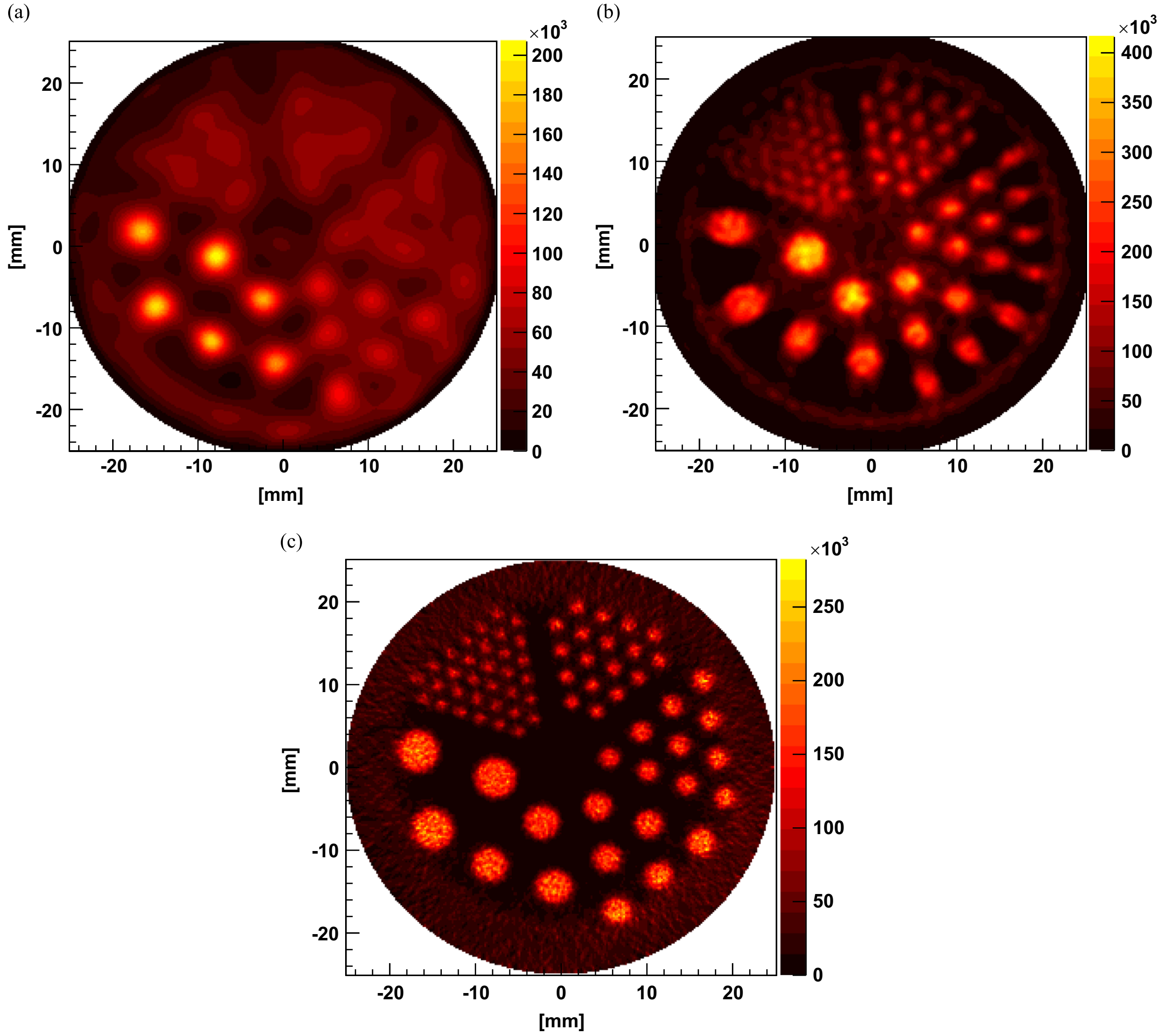

Fig. 7. Reconstructions of a Jaszczak phantom for three coincidence types: (a) 9.1 M BGO–BGO events (MSE=6.0), (b) 9.1 M Si–BGO events (MSE=4.1), (c) 8.4 M Si–Si events (MSE=3.3). The hot ring around the rods is not visible in the image reconstructed from Si–Si events as it is just outside the FOV of the modules.

4. Discussion

We developed a high resolution PET insert module and investigated the impact of adding different amounts of higher resolution information to standard PET data. The aim was to estimate an improvement in reconstructed image quality of the combined system that can be expected by using an insert with higher spatial resolution but lower efficiency than the standard PET ring. Depending on its geometry, inclusion of the high-resolution insert adds two new types of coincidence events. Both show substantial impact when included even in relatively small amounts of a few % (Figs. 8 and 10). The proposed insert can in principle be used in combination with any clinical PET scanner and due to silicon's low attenuation coefficient for 511 keV photons is not expected to influence its performance.

Silicon was chosen as a detector material for the insert as it enables construction of detectors with excellent spatial and energy resolutions. Due to their segmentation, silicon pad detectors are not susceptible to DOI effect and should be able to operate unperturbed in a magnetic field. A modular approach was adopted to achieve high versatility, allowing for customization both in terms of balancing trade-offs between detection efficiency, spatial, and timing resolution for task-specific requirements, and in positioning geometry, which can be tailored to the surface anatomy of the imaged region (e.g. for imaging of head and neck, breast and prostate areas).

At the present it is not clear how inserts should be used – either to boost efficiency of the additional detectors or to preserve performance of the outer detector. We have shown that a small portion of high-resolution data on the order of a few percent can already make a substantial improvement in image quality. Despite low stopping power of silicon sensors at 2% per mm of thickness, they could provide sufficient efficiency for usage in PET insert arrangement.

To estimate the relative efficiency of the insert module compared to the outer ring, Monte-Carlo simulations were performed using GEANT4 toolkit [25]. Two detectors were simulated: Lutetium orthosilicate (LSO) ring (80 cm diameter, 16 cm width and 2 cm thickness), and a single 1 mm thick silicon sensor. A clear tendency was found for clean events (i.e. events that were not scattered prior to interacting in the detector) to excite more energetic electrons, facilitating an implementation of an energy threshold (100 keV in the discussed study) for optimized event classification. The relative frequency for clean Si–LSO events compared to clean LSO–LSO events, was estimated to be

- 1% for annihilations close to the insert module, falling to.
- $\le 0.1\%$ for events originating deeper than ~ 10 cm within the body.

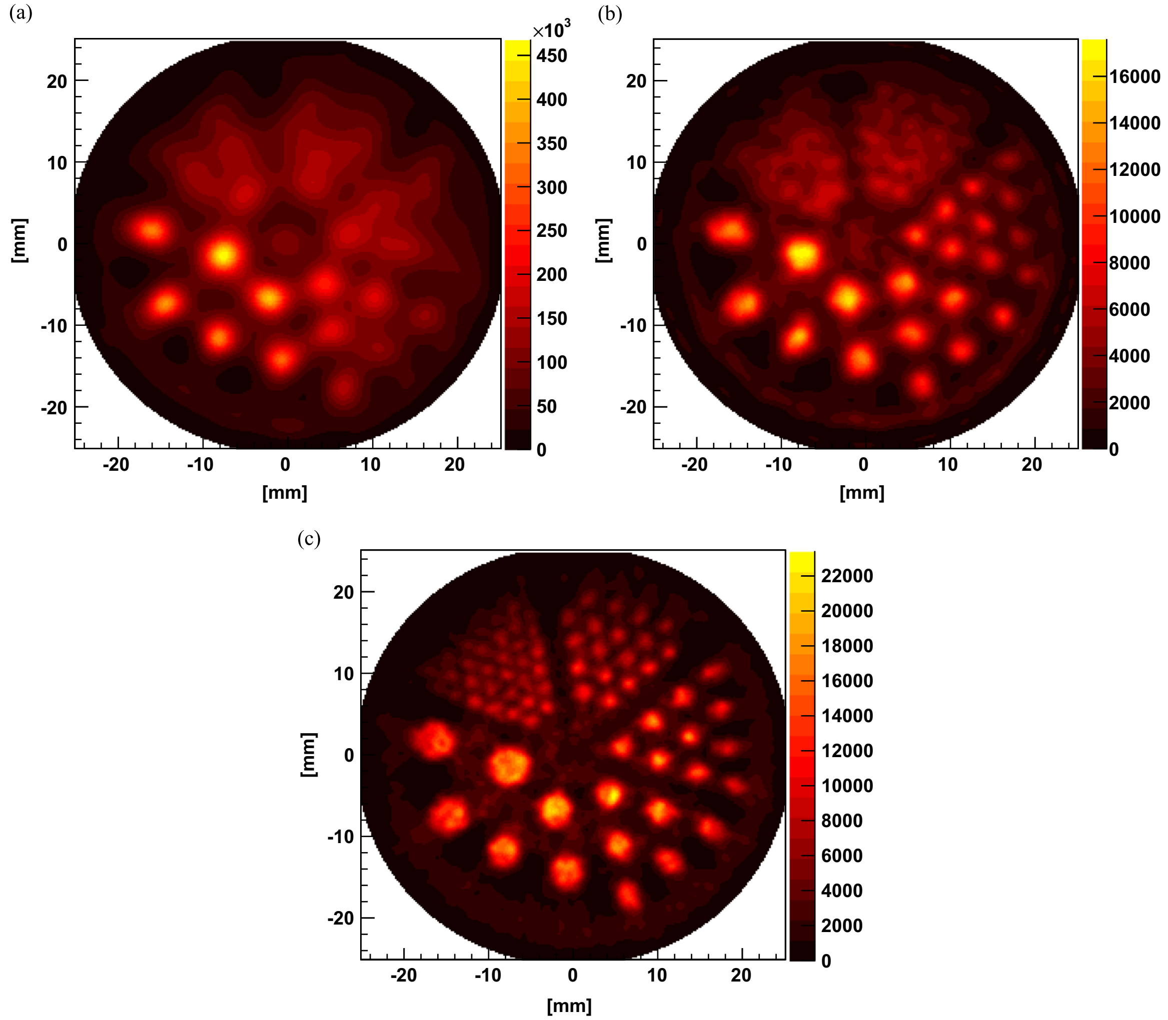

Fig. 8. Adding 3.5% of higher resolution events with a full angular coverage to 14 MB GO-BGO events, shown in (a) (MSE = 6.0): (b) Si–BGO (MSE = 4.9), and (c) Si–Si (MSE = 3.9).

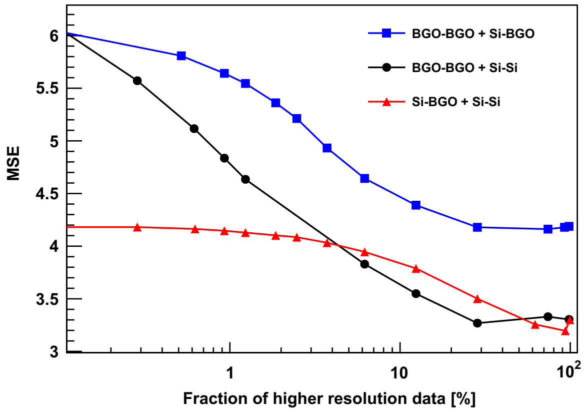

Fig. 9. Image quality as assessed by a MSE value, for different combinations of higher resolution Si–Si or Si–BGO events added to BGO–BGO events. MSE value is plotted as a function of the fraction of higher resolution data. A total of 8 M events were used for each combination (i.e. the ratio of 1% means that 80 k higher- and 7920 k lower resolution events were combined). (For interpretation of the references to color in this figure caption, the reader is referred to the web version of this paper.)

Thus, close to 1% relative efficiency per 1 mm of active silicon thickness for regions close to the insert could be expected in a clinical situation where high-resolution detectors would be positioned within the standard PET ring. Similar efficiencies have also been reported by [29]. Based on those results, reconstructed image quality such as shown in Fig. 10b can be achieved at a moderate technological expense by positioning two modules perpendicularly to each other, close to the region of interest, with the assumption that both silicon sensors that comprise a module are read out (in the evaluation setup, only one of the two silicon sensors was used in 2D geometry). While timing and foundries limit unit thickness to 0.5–1 mm range, stacks of few sensors could achieve required efficiency at moderate technological expense. The number of layers in the stack would be optimized for a single Compton interaction [5] to prevent uncertainty in the determination of the interaction position. The optimized stack would achieve efficiency in the 10–15% range. In a rare case of double interaction, Compton reconstruction algorithms could potentially be used [30], which would also help in recognition of events where photons scattered in the object prior to interacting in the sensors.

Traditionally, energy of the photon interaction is used to separate clean events depositing 511 keV after photo-absorption from those where photons were scattered in the object prior to interaction, depositing smaller amounts of energy. Since Compton interactions dominate in silicon sensors, no such distinction can be made, and lowering threshold to 20 keV in our study was used to improve the detection efficiency. Previous reports demonstrate that a vague distinction between direct and scattered photons can be made for

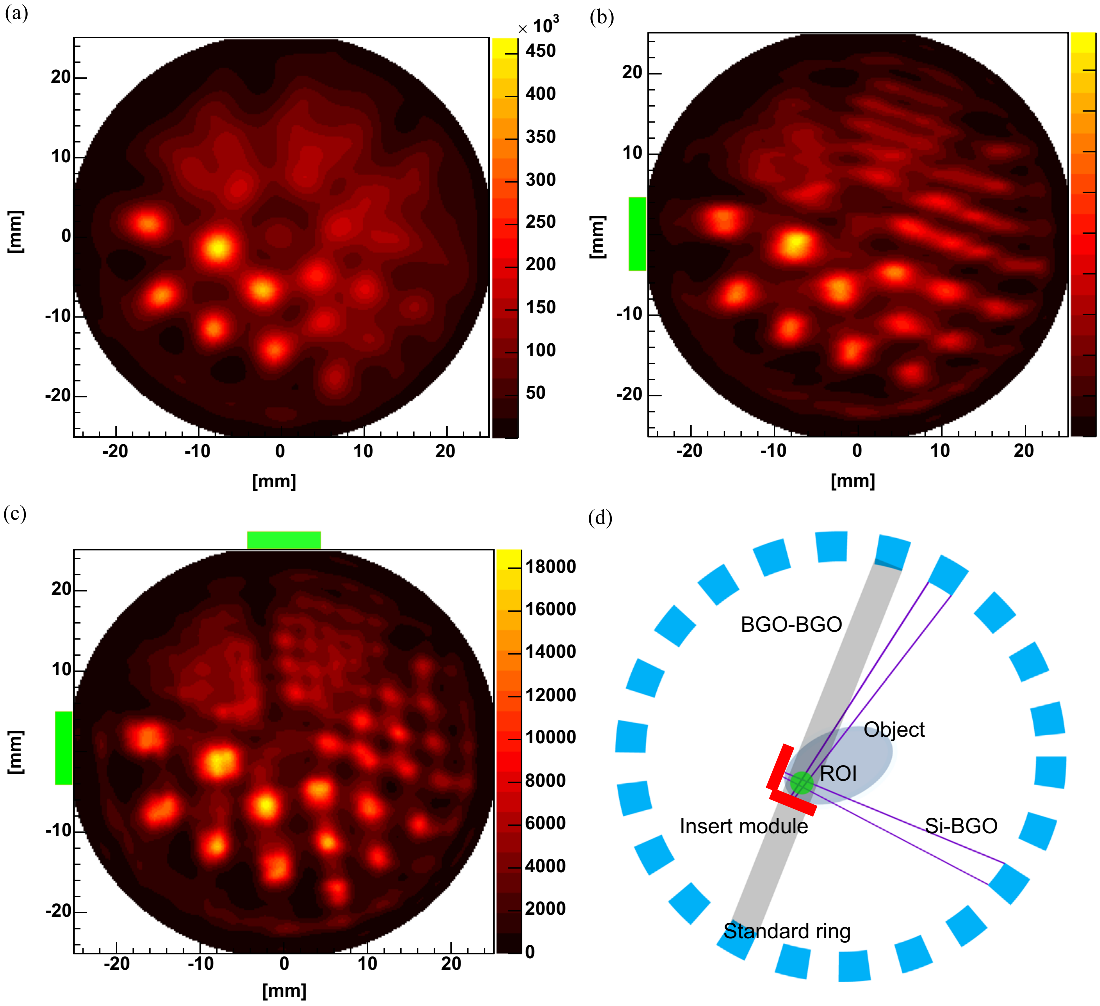

Fig. 10. Effect of adding 3% of Si–BGO events with limited angular coverage to 14 M BGO-BGO events, shown in (a) (MSE=6.0): (b) single module (MSE=5.4), and (c) perpendicular arrangement (MSE=4.9). Positions of the two modules are for illustrative purposes highlighted in green. Angular coverage for each module was 36°. Illustration of the perpendicular arrangement is shown in (d). (For interpretation of the references to color in this figure caption, the reader is referred to the web version of this paper.)

Compton interactions [25]. When the energy of the excited Compton electron was below approximately 100 keV, the event was more likely to be caused by a photon that has undergone a prior Compton scattering in the object. In our study, the object was sufficiently small making contribution from scattered events manageable even when using low energy threshold.

Timing of present silicon sensors was not optimized for high count-rate environments. On top of jitter and time-walk, which are minimized for shorter shaping times, silicon sensors suffer from additional interaction location related broadening. For clinical application, the latter can be minimized by reducing sensor thickness and increasing sensor bias. Both serve to speed the sweeping of charge carriers to signal electrodes. A possible solution to maintain the ratio of pixel volume per electronic channel would be to vertically connect aligned pixels of a pair of flipped sensors with halved thickness. Previous studies have shown that by combining these two strategies, activities of ~50–100 MBq within the FOV of the insert can be handled effectively [24,25].

5. Conclusion

We constructed a demonstration setup for the evaluation of the high-resolution PET insert module, where we acquired data using a Jaszczak phantom, combining three types of coincidence events. Our results suggest a substantial improvement in reconstructed image quality when adding a few % of higher resolution data, which should be attainable in a clinical setting by using an equivalent of two insert modules (effective sensor thickness of 4 mm).

Acknowledgements

The work was partially carried out within the EURATOM Seventh Framework Programme collaborative project MADEIRA, co-funded by the European Commission through Grant agreement FP7-212100. Authors would also like to acknowledge support from the NIH (R01 EB430-37).

References

[1] W.A. Weber, Radiotherapy Oncology 96 (3) (2010) 308.
[2] B. Bai, J. Bading, P.S. Conti, Theranostics 3 (10) (2013) 787.
[3] W.W. Moses, Nuclear Instruments and Methods in Physics Research Section A: Accelerators, Spectrometers, Detectors and Associated Equipment 648 (2011) 236.
[4] C.S. Levin, Journal of Nuclear Medicine 53 (2) (2012) 167.
[5] S.J. Park, W.L. Rogers, N.H. Clinthorne, Physics in Medicine & Biology 52 (15) (2007) 4653.
[6] V. Schulz, Y. Berker, A. Berneking, N. Omidavri, F. Kiessling, A. Gola, C. Piemonte, Physics in Medicine & Biology 58 (14) (2013) 4733.
[7] S. Seifert, G. van der Lei, H.T. van Dam, D.R. Schaart, Physics in Medicine & Biology 58 (9) (2013) 3061.

[8] A.V. Stolin, S. Majewski, G. Jaliparthi, R.R. Raylman, IEEE Transactions on Nuclear Science NS-60 (1) (2013) 82.
[9] R.R. Raylman, A.V. Stolin, S. Majewski, J. Proffitt, Nuclear Instruments and Methods in Physics Research Section A: Accelerators, Spectrometers, Detectors and Associated Equipment 735 (2014) 602.
[10] H. Peng, C.S. Levin, Physics in Medicine & Biology 55 (9) (2010) 2761.
[11] S. Komarov, Y. Yin, H. Wu, J. Wen, H. Krawczynski, L.J. Meng, Y.C. Tai, Physics in Medicine & Biology 57 (22) (2012) 7355.
[12] Y.C. Tai, H. Wu, D. Pal, J. O'Sullivan, Journal of Nuclear Medicine 49 (3) (2008) 471.
[13] H. Wu, D. Pal, J.A. O'Sullivan, Y.C. Tai, Journal of Nuclear Medicine 49 (1) (2008) 79.
[14] A.J. Mathews, S. Komarov, H. Wu, J.A. O'Sullivan, Y.C. Tai, Physics in Medicine & Biology 58 (18) (2013) 6407.
[15] J. Zhou, J. Qi, Physics in Medicine & Biology 54 (17) (2009) 5193.
[16] J. Qi, Y. Yang, J. Zhou, Y. Wu, S.R. Cherry, Physics in Medicine & Biology 56 (17) (2011) 165.
[17] N.H. Clinthorne, E. Cochran, E. Chesi, M. Grkovski, B. Grošičar, K. Honscheid, S. Huh, H. Kagan, C. Lacasta, K. Brzezinski, V. Linhart, M. Mikuž, S. Smith, A. Studen, V. Stankova, P. Weilhammer, D. Žontar, Physics Procedia 37 (2012) 1488.
[18] N.H. Clinthorne, K. Brzezinski, E. Chesi, V. Cindro, E. Cochran, M. Grkovski, B. Grošičar, K. Honscheid, S. Huh, H. Kagan, C. Lacasta, V. Linhart, M. Mikuž, S. Smith, V. Stankova, A. Studen, P. Weilhammer, D. Žontar, Nuclear Instruments and Methods in Physics Research Section A: Accelerators, Spectrometers, Detectors and Associated Equipment 699 (21) (2013) 216.
[19] A. Studen, K. Brzezinski, E. Chesi, V. Cindro, N.H. Clinthorne, M. Grkovski, B. Grošičar, K. Honscheid, H. Kagan, C. Lacasta, G. Llosa, M. Mikuž, V. Stankova, P. Weilhammer, D. Žontar, Nuclear Instruments and Methods in Physics Research Section A: Accelerators, Spectrometers, Detectors and Associated Equipment 702 (2013) 88.
[20] J. Straver., O. Toker, P. Weilhammer, C. Colledani, W. Dulinski, R. Turchetta, L. Bosisio, Nuclear Instruments and Methods in Physics Research Section A: Accelerators, Spectrometers, Detectors and Associated Equipment 348 (2) (1994) 485.
[21] E. Steinbauer, P. Bauer, M. Gerteschlager, G. Bortels, J.P. Biersack, P. Burger, Nuclear Instruments and Methods in Physics Research Section B: Beam Interactions with Materials and Atoms 85 (1–4) (1994) 642.
[22] D. Burdette, D. Albani, E. Chesi, N.H. Clinthorne, E. Cochran, K. Honscheid S.S. Huh, H. Kagan, M. Knopp, C. Lacasta, M. Mikuž, P. Schmalbrock, A. Studen, P. Weilhammer, Nuclear Instruments and Methods in Physics Research Section A: Accelerators, Spectrometers, Detectors and Associated Equipment 609 (2–3) (2009) 263.
[23] B. Weissler, P. Gebhardt, C.W. Lerche, J. Wehner, T. Solf, B. Goldschmidt J.E. Mackewn, P.K. Marsden, F. Kiessling, M. Perkuhn, D. Heberling, V. Schulz, Physics in Medicine & Biology 59 (17) (2014) 5119.
[24] A. Studen, D. Burdette, E. Chesi, V. Cindro, N.H. Clinthorne, E. Cochran, B. Grošičar, H. Kagan, C. Lacasta, V. Linhart, M. Mikuz, V. Stankova, P. Weilhammer, D. Žontar, Radiation Protection Dosimetry 139 (2010) 199.
[25] A. Studen, E. Chesi, V. Cindro, N.H. Clinthorne, E. Cochran, B. Grošičar, K. Honscheid, H. Kagan, C. Lacasta, G. Llosa, V. Linhart, M. Mikuz, V. Stankova, P. Weilhammer, D. Žontar, Nuclear Instruments and Methods in Physics Research Section A: Accelerators, Spectrometers, Detectors and Associated Equipment 648 (2011) S255.
[26] A. Studen, K. Brzezinski, E. Chesi, V. Cindro, N.H. Clinthorne, M. Grkovski, B. Grošičar, K. Honscheid, S.S. Huh, H. Kagan, C. Lacasta, G. Llosa, M. Mikuž, S. Smith, V. Stankova, P. Weilhammer, D. Žontar, IEEE Nuclear Science Symposium Conference Record, 2012, pp. 1305–1310.
[27] D. Burdette, A study of the effects of stron magnetic fields on the image resolution of PET scanners (Ph.D. dissertation), Department of Physics, Ohio State University, 2009.
[28] L.A. Shepp, Y. Vardi, IEEE Transactions on Medical Imaging 1 (2) (1982) 113.
[29] K. Brzezinski, J.F. Oliver, J. Gillam, M. Rafecas, Physics in Medicine & Biology 59 (20) (2014) 6117.
[30] A. Zoglauer, S.E. Boggs, Application of neural networks to the identification of the compton interaction sequence in compton imagers, in: IEEE Nuclear Science Symposium Conference Record, 2007, pp. 4436–4441.